

Subsalt velocity analysis by target-oriented wavefield tomography: A 3-D field-data example

Yaxun Tang and Biondo Biondi

ABSTRACT

We apply target-oriented wavefield tomography to a 3-D field data set acquired from the Gulf of Mexico. Instead of using the original surface-recorded data set, we use a new data set synthesized specifically for velocity analysis to update subsalt velocities. The new data set is generated based on an initial unfocused target image and by a novel application of 3-D generalized Born wavefield modeling, which correctly preserves velocity kinematics by modeling non-zero subsurface-offset-domain images. We show that the target-oriented inversion strategy drastically reduces the data size and the computation domain for 3-D wavefield tomography, greatly improving its efficiency and flexibility. We apply differential semblance optimization (DSO) using the synthesized new data set to optimize subsalt velocities. The updated velocity model significantly improves the continuity of subsalt reflectors and yields flattened angle-domain common-image gathers.

INTRODUCTION

Accurate reflectivity imaging requires an accurate background velocity model. As seismic exploration moves towards structurally complex areas, wavefield-based tomography that better models band-limited wave phenomena becomes necessary for high-quality velocity model building. Wavefield-based tomography, however, is still expensive for industrial-scale applications (Biondi and Sava, 1999; Shen et al., 2005; Albertin et al., 2006; Fei et al., 2009), both because the method uses more expensive wavefield modeling engines, and because it lacks flexibility and usually requires the use of the whole recorded data set for velocity analysis.

To reduce the cost and increase the flexibility of wavefield-based tomography, Biondi (2006); Guerra (2010); Tang and Biondi (2010) originated the idea of target-oriented wavefield tomography. The idea is to synthesize a target-oriented new data set specifically for velocity analysis. The new data set is designed to be much smaller than the original surface-recorded data set, while still containing all necessary information for velocity updating. This strategy allows us to apply the powerful but expensive wavefield-based technique only in areas where it is necessary, such as in subsalt regions with complex overburdens, and leave areas with relatively simple geologies to be handled by conventional velocity-analysis methods, which are sufficient to produce accurate results.

By localizing the computation within a selected target zone, the target-oriented inversion strategy dramatically improves the efficiency and flexibility of wavefield-based tomography. Therefore, it can greatly shorten the cycle time from seismic processing to interpretation, enabling interpretation-driven interactive wavefield-based velocity analysis, where different geological scenarios can be tested in almost real time (Halpert et al., 2008). The high efficiency may also make velocity uncertainty analysis feasible, which requires inverting velocity models multiple times to build the probability distribution (Tarantola, 2005).

Biondi (2006); Guerra et al. (2009); Guerra (2010) synthesize a new data set for local tomography using the concept of prestack exploding-reflector modeling (PERM). PERM, however, generates crosstalk when multiple image events (reflectors) are modeled simultaneously. This limits the number of reflectors it can model. Manual picking and stochastic encoding methods, such as random-phase encoding, are required to mitigate the impact of the crosstalk.

In contrast, Tang and Biondi (2010) formulate the problem under a seismic-data-mapping (SDM) framework (Hubral et al., 1996; Bleistein and Jaramillo, 2000) and use generalized Born wavefield modeling as the mapping operator to synthesize a new data set for velocity analysis. Generalized Born wavefield modeling is extended from conventional Born modeling (Stolt and Benson, 1986) to include modeling of the non-zero subsurface offset images. As shown by Tang and Biondi (2010), the inclusion of the subsurface offset in the modeling process preserves the correct velocity information and is crucial to the success of this method. One advantage of generalized Born wavefield modeling is that it does not require any picking, but picking can be incorporated if it is desired. Another advantage is that it can model arbitrary number of reflectors simultaneously and is minimally affected by crosstalk artifacts.

In this paper, we follow the method of Tang and Biondi (2010) and use generalized Born wavefield modeling to generate a target-oriented data set for local velocity analysis. In the subsequent sections, we first review the theory of target-oriented tomography using synthesized Born data. We then apply the methodology to a 3-D field data set acquired from the Gulf of Mexico (GOM), where we update the subsalt velocities in a target-oriented fashion.

THEORY

We formulate our method under the framework of seismic data mapping (SDM) (Hubral et al., 1996; Bleistein and Jaramillo, 2000), where the idea is to transform the original observed seismic data from one acquisition configuration to another with a designed mapping operator. SDM can be summarized as two main steps: (1) apply the (pseudo) inverse of the designed mapping operator to the original data set to generate a model, and (2) apply the forward mapping operator to the model to generate a new data set with a different acquisition configuration than the original one.

In our case, we use generalized Born wavefield modeling to perform data mapping.

With an initial velocity model, seismic prestack images can be obtained using the pseudo-inverse of the generalized Born modeling operator as follows:

$$\mathbf{m} = \mathbf{H}_0^\dagger \mathbf{L}_0^* \mathbf{d}_{\text{obs}}, \quad (1)$$

where $*$ and † denote adjoint and pseudo-inverse, respectively; \mathbf{m} is the seismic image; \mathbf{L}_0 is the generalized Born modeling operator computed using an initial velocity model \mathbf{v}_0 , whose adjoint \mathbf{L}_0^* is the well-known depth migration operator; \mathbf{H}_0 is the Hessian operator (Plessix and Mulder, 2004; Valenciano, 2008; Tang, 2009); and \mathbf{d}_{obs} is the observed surface data.

It is important to note that the seismic image \mathbf{m} must be parameterized as a function of both spatial location and some prestack parameter, such as the subsurface offset, reflection angle, etc., in order to preserve the velocity information for later velocity analysis (Tang and Biondi, 2010). In this paper, we use the subsurface offset as our prestack parameter. The significance of the Hessian operator in equation 1 is that its pseudo-inverse removes the influence of the original acquisition geometry in the least-squares sense, and the resulting image is independent from the original data. However, the full Hessian \mathbf{H}_0 is impossible to obtain in practice due to its size and computational cost; we therefore approximate it by a diagonal matrix : $\mathbf{H}_0 \approx \text{diag}\{\mathbf{H}_0\}$. We further reduce the cost of computing the diagonal of Hessian by using the phase encoding method (Tang, 2007, 2009; Tang and Lee, 2010).

We obtain a target image $\mathbf{m}_{\text{target}}$ by applying a selecting operator \mathbf{S} to the initial image: $\mathbf{m}_{\text{target}} = \mathbf{S}\mathbf{m}$, where the selecting operator \mathbf{S} can be simply a windowing operator. A new data set $\tilde{\mathbf{d}}_{\text{obs}}$ can then be simulated as follows:

$$\tilde{\mathbf{d}}_{\text{obs}} = \tilde{\mathbf{L}}_0 \mathbf{m}_{\text{target}}, \quad (2)$$

where $\tilde{\mathbf{L}}_0$ is the Born modeling operator computed using the same initial velocity \mathbf{v}_0 , but with a different acquisition configuration. The wavefield propagation can be restricted to regions with inaccurate velocities, and the modeled data can be collected at the top of the target region. The target-oriented modeling strategy makes the new data set much smaller than the original one. The new data set can be imaged using the migration operator, i.e., the adjoint of $\tilde{\mathbf{L}}$, with an arbitrary velocity \mathbf{v} , as follows:

$$\widehat{\mathbf{m}}_{\text{target}} = \tilde{\mathbf{L}}^* \tilde{\mathbf{d}}_{\text{obs}}. \quad (3)$$

We pose the velocity estimation problem as an optimization problem that seeks an optimum velocity model by minimizing a user-defined image residual (or maximizing some measure of the image coherence). There are many ways of defining the objective functions. In this paper, we use the differential semblance optimization (DSO) (Symes and Carazzone, 1991) as the criterion to estimate the velocity. The DSO objective function in the subsurface-offset domain is (Shen, 2004; Shen and Symes, 2008)

$$F(\mathbf{v}) = \frac{1}{2} \sum_{\mathbf{x}} \sum_{\mathbf{h}} |\mathbf{h}|^2 \widehat{m}_{\text{target}}^2(\mathbf{x}, \mathbf{h}), \quad (4)$$

where $\mathbf{x} = (x, y, z)$ is the image point in the subsurface and $\mathbf{h} = (h_x, h_y, 0)$ is the subsurface offset. The physical interpretation of the subsurface-offset-domain DSO is that it optimizes the velocity model by penalizing energy at non-zero subsurface offset, taking advantage of the fact that seismic events should focus at zero-subsurface offset if migrated using an accurate velocity model (Shen, 2004). However, the gradient of the objective function defined by equation 4 is sensitive to the amplitude variation of the images due to uneven illumination (Vyas and Tang, 2010; Fei and Williamson, 2010). We propose to normalize the DSO objective function by the square of the root-mean-squared (RMS) image amplitudes to reduce the influence of image amplitude variations. The normalized DSO objective function is

$$J(\mathbf{v}) = \frac{1}{2} \sum_{x,y} \frac{\sum_{z,\mathbf{h}} |\mathbf{h}|^2 |\widehat{m}_{\text{target}}(\mathbf{x}, \mathbf{h})|^2}{\sum_{z,\mathbf{h}} |\widehat{m}_{\text{target}}(\mathbf{x}, \mathbf{h})|^2}. \quad (5)$$

We use nonlinear conjugate-gradient method to minimize J . The gradient is calculated using the adjoint-state method (with a one-way wave-equation formulation) without explicitly computing the Jacobian matrix (Shen and Symes, 2008; Sava and Vlad, 2008; Tang et al., 2008).

3-D FIELD-DATA EXAMPLES

We apply the target-oriented wavefield tomography to a data set acquired from the Gulf of Mexico (GOM). The data set was acquired using a narrow-azimuth towed streamer (NATS) acquisition system, and further rotated using azimuth moveout (AMO) (Biondi et al., 1998) into zero azimuth. The minimum and maximum inline offsets are 0.3 km and 8.2 km, respectively. The frequency content of the data set ranges between 5 Hz and 35 Hz. The initial 3-D velocity model is shown in Figure 1. Velocities above the target (outlined by a black box) and the salt interpretation are known to be accurate. The goal is to invert for subsalt velocities inside the target region. The initial velocities inside the box are set to be $v(z)$.

Generating initial image gathers

We perform conical-wave migration (Whitmore, 1995; Duquet et al., 2001; Zhang et al., 2005; Liu et al., 2006) to generate the initial image gathers, where we synthesize 101 conical waves for each crossline and migrate 12625 conical waves in total. The minimum and maximum inline take-off angles at the surface for the conical waves are -30° and 30° , respectively. The maximum frequency used for the initial migration is 20 Hz. We also compute the diagonal of the Hessian in the conical-wave domain using the phase-encoding method (Tang, 2009), which encodes the source-side Green's functions using inline plane-wave phase-encoding functions and the receiver-side Green's functions using random-phase encoding functions. The simultaneous encoding dramatically reduces the computational cost of the Hessian (Tang and Biondi, 2011).

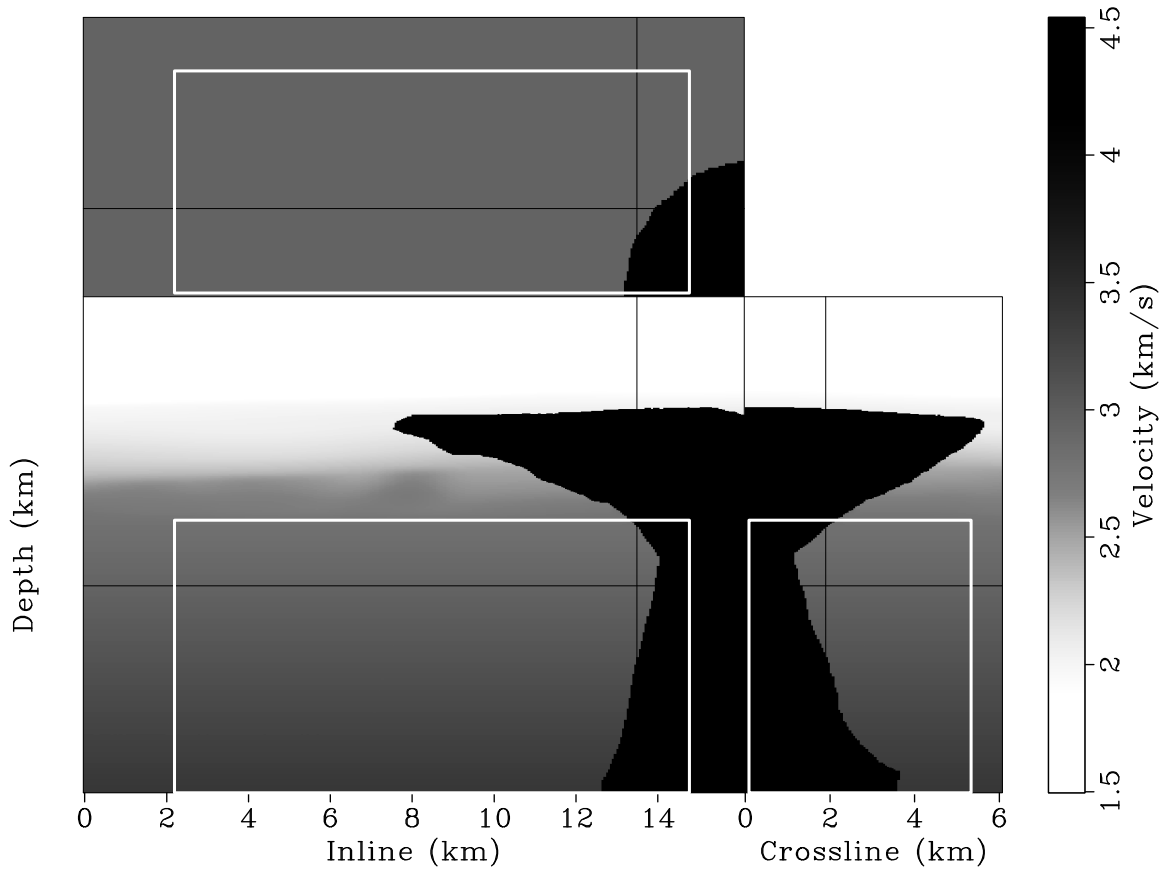


Figure 1: The initial 3-D velocity model. The black box outlined area is the target region for velocity analysis. Velocities above the target region and the salt interpretation are known to be accurate. [ER]

Figure 2 shows the zero-subsurface offset image for the target region obtained using the initial velocity model (Figure 1). The image has been normalized with the diagonal of the Hessian (not shown here). To more accurately preserve the velocity information, we compute both inline and crossline subsurface offsets (Figure 3). The crossline subsurface offset is included because wavefields can travel out of plane during propagation, and therefore they may image the subsurface with different azimuths than that on the surface. The 3-D subsurface-offset-domain common-image gathers (SODCIGs) shown in Figure 3 confirm this; the events in the top panels of Figures 3a and 3b are tilted, suggesting that they are not imaged by zero subsurface azimuth. Also note that the 3-D SODCIGs are not well focused at the zero subsurface offset in either the inline or crossline directions. The defocusing in the inline subsurface offset (h_x) is mainly caused by velocity inaccuracies, whereas the defocusing in the crossline subsurface offset (h_y) is mainly due to insufficient crossline data coverage (single surface azimuth data)(Tang, 2007).

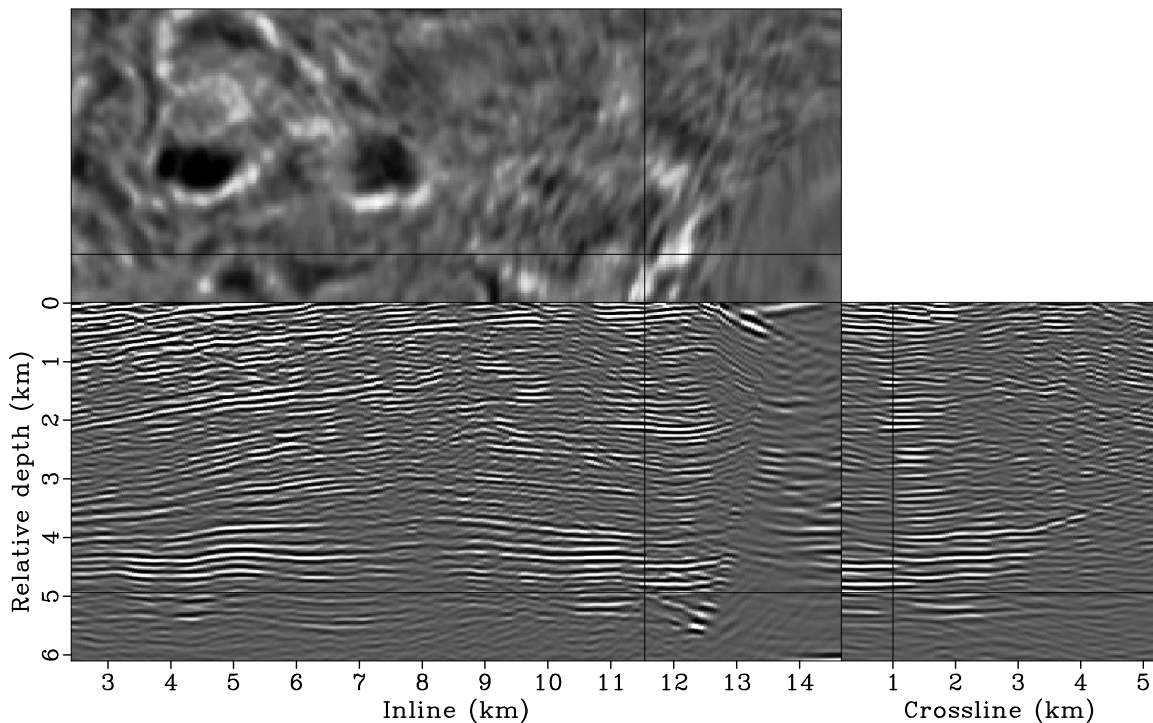


Figure 2: The zero-subsurface-offset-domain image migrated using the original data set and the initial velocity. The image has been normalized using the diagonal of the phase-encoded Hessian. [CR]

3-D Born wavefield modeling

The next step is to model a new data set for velocity analysis. The initial image and gathers (Figures 2 and 3) have been preprocessed before the modeling step, where we simply mute events inside the salt body. More sophisticated preprocessing,

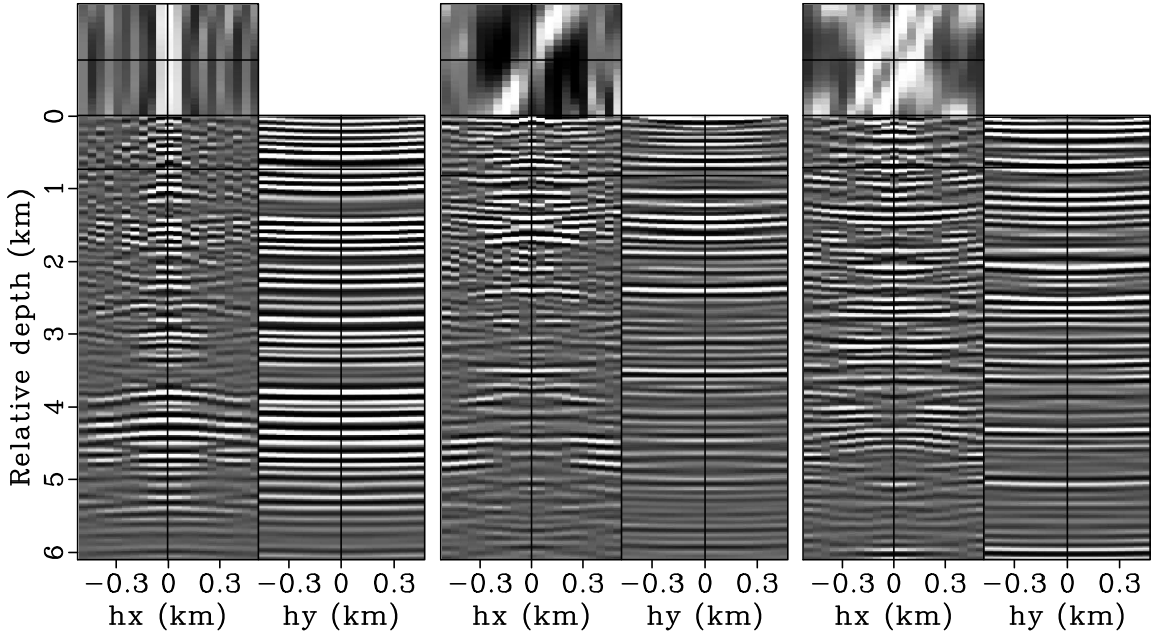


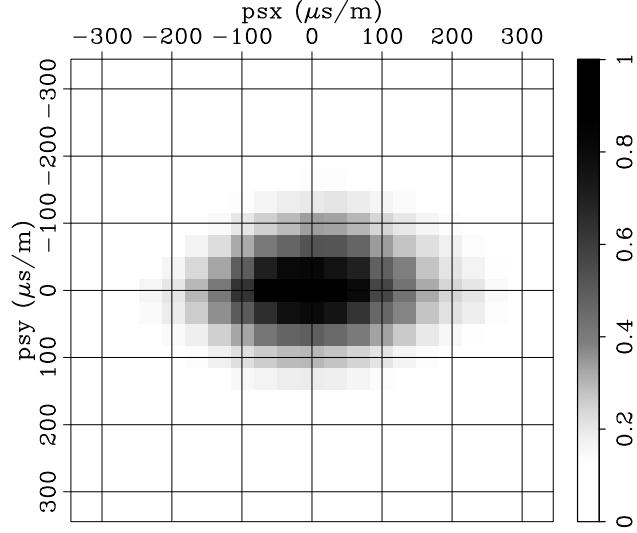
Figure 3: The Hessien-normalized 3-D SODCIGs obtained using the original data set and the initial velocity model. Panels (a), (b) and (c) are extracted at (3.04, 1.34) km, (6.09, 2.86) km and (9.13, 4.38) km, respectively. [CR]

such as noise attenuation, key reflection selection, etc., can also be applied. The preprocessing step allows human interaction in the velocity analysis workflow, adding desired flexibility and control to this method.

We use 3-D plane-wave modeling to generate a Born data set at the top of the target region. To determine the optimum parameters for the 3-D modeling, we carry out seismic visibility analysis (Jin and Xu, 2010), which can provide us a quantitative estimate of which part of the data contributes most to the target region for a given prestack acquisition geometry. Figure 4 shows the average source visibility map for the dominant frequency 10 Hz, as a function of both inline and crossline ray parameters. Note that most of the energy contributing to the target region falls within the range where $\tilde{p}_{sx} \in (-213, 213) \mu\text{s/m}$, and $\tilde{p}_{sy} \in (-180, 180) \mu\text{s/m}$.

Based on the result of visibility analysis, we modeled 315 plane waves at the top of the target region, with 21 plane waves inline and 15 plane waves crossline. The minimum and maximum dip and azimuth angles of these plane waves are approximately -47.7° and 47.7° , -40.2° and 40.2° , respectively. The dominant frequency used for the generalized Born wavefield modeling is 10 Hz. Figure 5 shows a 3-D plane-wave source function with both incident dip and azimuth angles equal to 10° , shooting from the top of the target region (Figure 1), and the corresponding 3-D plane-wave gather collected at the top of the target region.

Figure 4: The average source visibility (data-domain illumination) for the target region using 3-D plane-wave acquisition geometry for the Born wavefield modeling. Note that most of the energy contributing to the target region falls within the range where $\tilde{p}_{s_x} \in (-213, 213)$, and $\tilde{p}_{s_y} \in (-180, 180)$. [CR]



Tomographic inversion

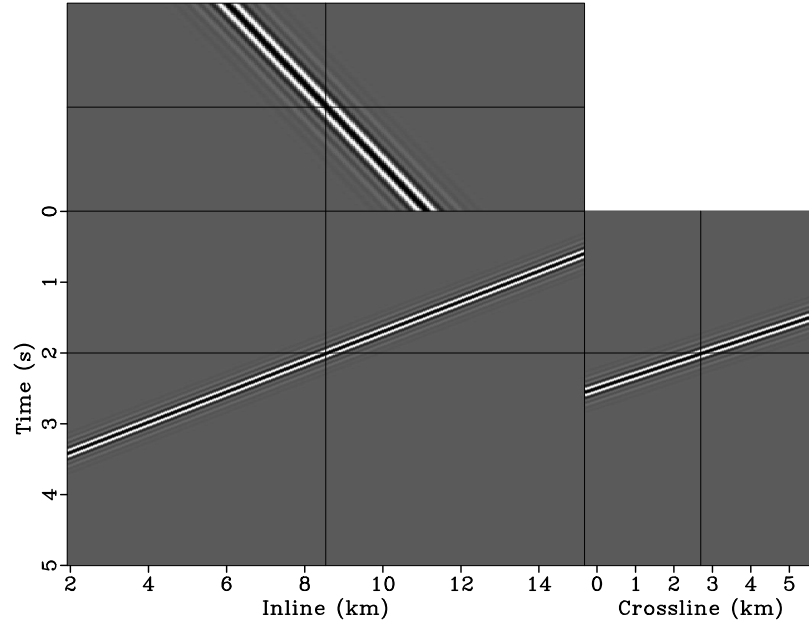
We use the normalized DSO (equation 5) to optimize the subsalt velocity. Although the 3-D Born data set is synthesized with both inline and crossline subsurface offsets, we use only inline subsurface offsets for velocity inversion due to the limited angular coverage in the crossline direction. We regularize the inversion by smoothing the gradient using a B-spline operator as follows:

$$\mathbf{g}_s = \mathbf{KBB}^* \mathbf{g}, \quad (6)$$

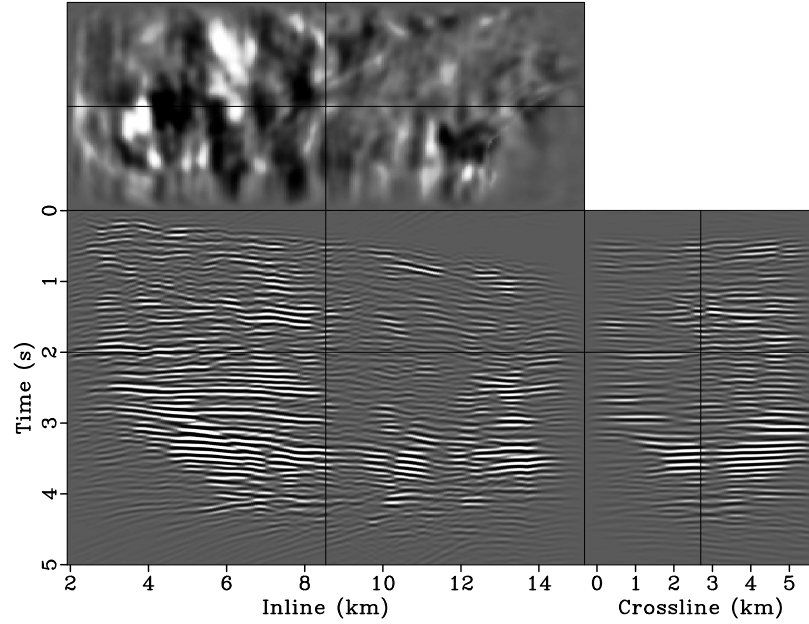
where \mathbf{g}_s and \mathbf{g} are the smoothed and raw gradient vectors, respectively; \mathbf{B} is the B-spline projection operator. The spacing of the B-spline nodes controls the smoothness of the velocity updates. A mask operator \mathbf{K} has been introduced to prevent updating the salt velocities (Figure 6).

Instead of using a fixed degree for gradient smoothing, we gradually decrease the smoothness of the gradient after every few iterations by decreasing the spacing of the B-spline nodes. We have found this strategy effective in finding an acceptable minimum, even when starting with a velocity model far from being accurate. Decreasing the smoothness of the gradient at later iterations also helps improve the resolution of the velocity model. This procedure is similar to the multi-scale inversion strategy, which has proven useful in practice (Bunks et al., 1995; Soubaras and Gratacos, 2007). Table 1 illustrates the spacings of the B-spline nodes for different iterations. Figures 7 presents the raw and smoothed gradients at different iterations.

We restart the nonlinear conjugate gradient solver every 10 iterations, and we terminate the inversion after 40 iterations when the objective function does not decrease significantly. Figure 8 shows how the objective function evolves over the first 40 iterations, whereas Figure 9 plots the step lengths as a function of iterations. It seems that the objective function converges very fast at the first several iterations,



(a)



(b)

Figure 5: The synthesized 3-D plane-wave data. Panel (a) is the plane-wave source function with both incident dip and azimuth angles equal 10° at the top of the target region shown in Figure 1, and (b) is the corresponding plane-wave gather collected also at the top of the target region. [CR]

Iterations	Node spacing in x	Node spacing in y	Node spacing in z
1 to 10	2.0 km	2.0 km	0.6 km
11 to 20	1.8 km	1.8 km	0.4 km
21 to 30	1.2 km	1.2 km	0.3 km
31 to 40	0.7 km	0.7 km	0.2 km

Table 1: The spacings of B-spline nodes for different iterations.

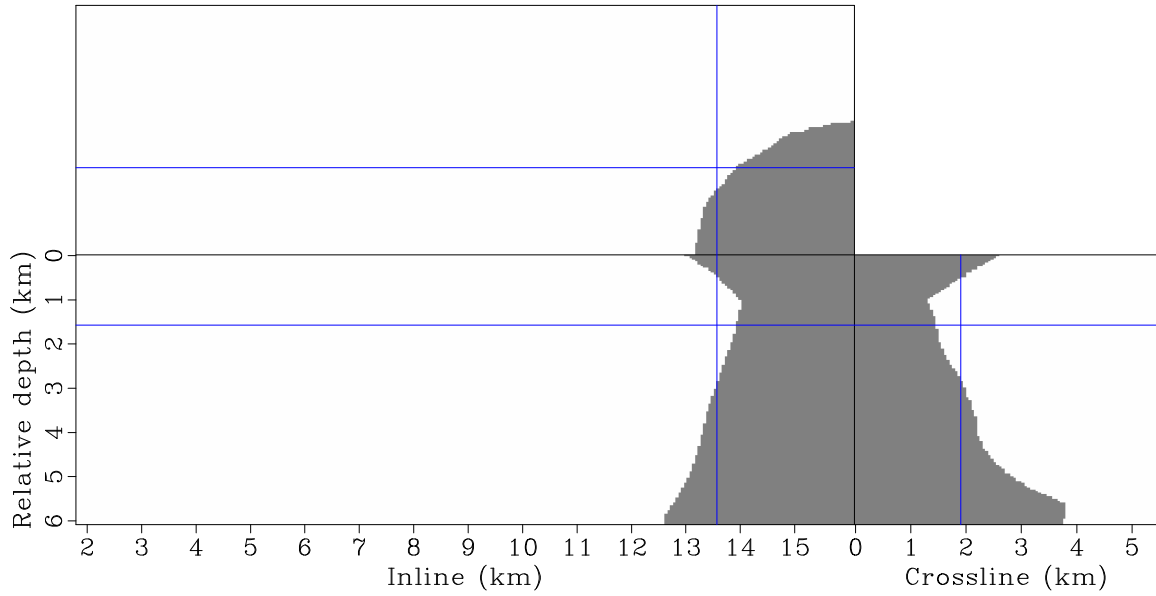


Figure 6: The mask operator applied to the gradient to prevent updating the velocity inside the salt. [CR]

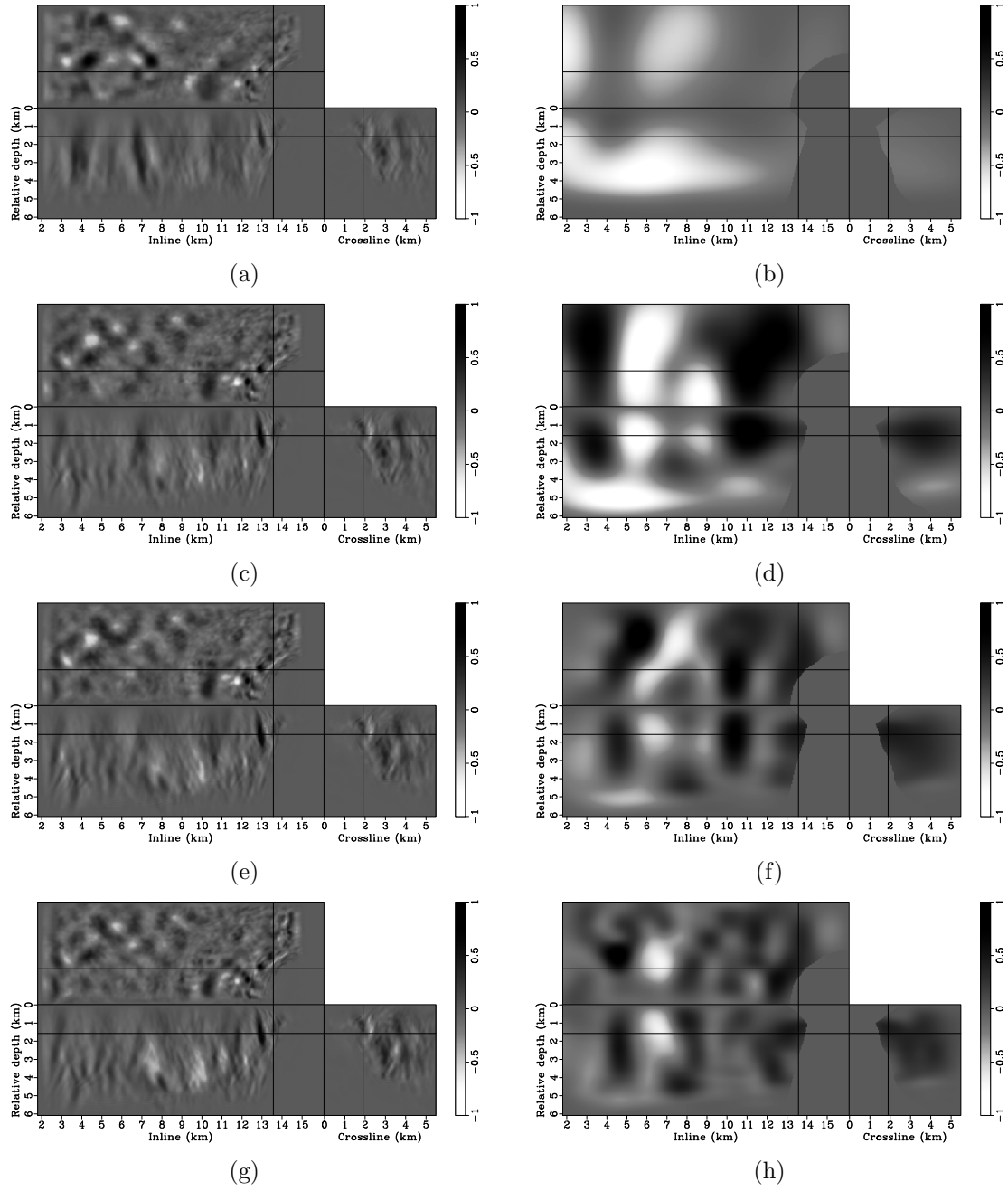


Figure 7: Panels (a), (c), (e), (g) are the raw gradients at iterations 1, 11, 21 and 31, respectively. Panels (b), (d), (f) and (h) are the corresponding gradients after applying the smoothing and mask operators. [CR]

then the convergence slows down quickly, and that the velocity model gets the most significant updates at the first several iterations.

The final velocity model obtained by merging the inverted velocity model in the target region with the velocity model above the target is shown in Figure 10. It is interesting to note that the velocities beneath the salt body are slightly lower than the surrounding sediment velocities. The low velocities might indicate overpressure due to the compaction of the salt body.

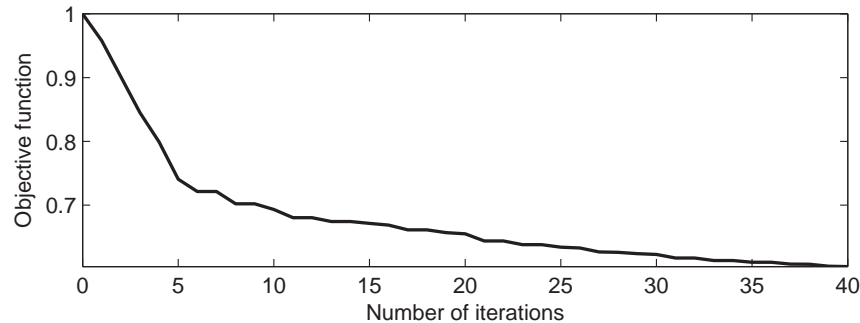


Figure 8: The evolution of the objective function over the first 40 DSO iterations. The objective function values have been normalized to 1. [CR]

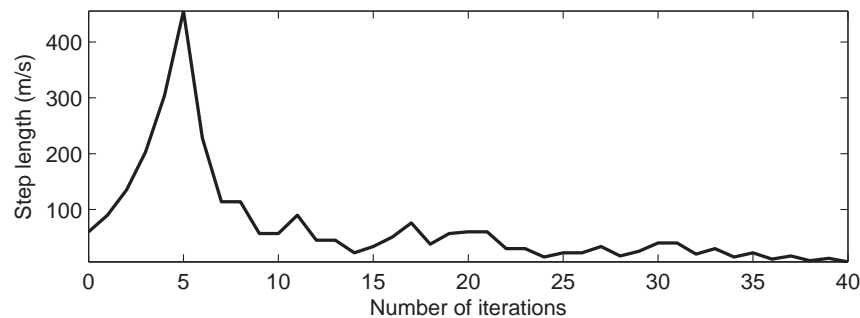


Figure 9: Step length versus the number of iterations. The initial step length is about 20 m/s. [CR]

Migrating the original data set using the updated velocity model

After the tomographic inversion step, we migrate the original data set using the updated velocity model. Once again, we perform 3-D conical wave migration and normalize the migrated image with the diagonal of the phase-encoded Hessian, also computed using the updated velocity model, to compensate for uneven subsurface illumination. The updated image (Figures 11(b), 12(b) and 13(b)) significantly improves the continuity of the reflectors in both the inline and crossline directions and is also more focused than the initial one (Figures 11(a), 12(a) and 13(a)). Figures 14,

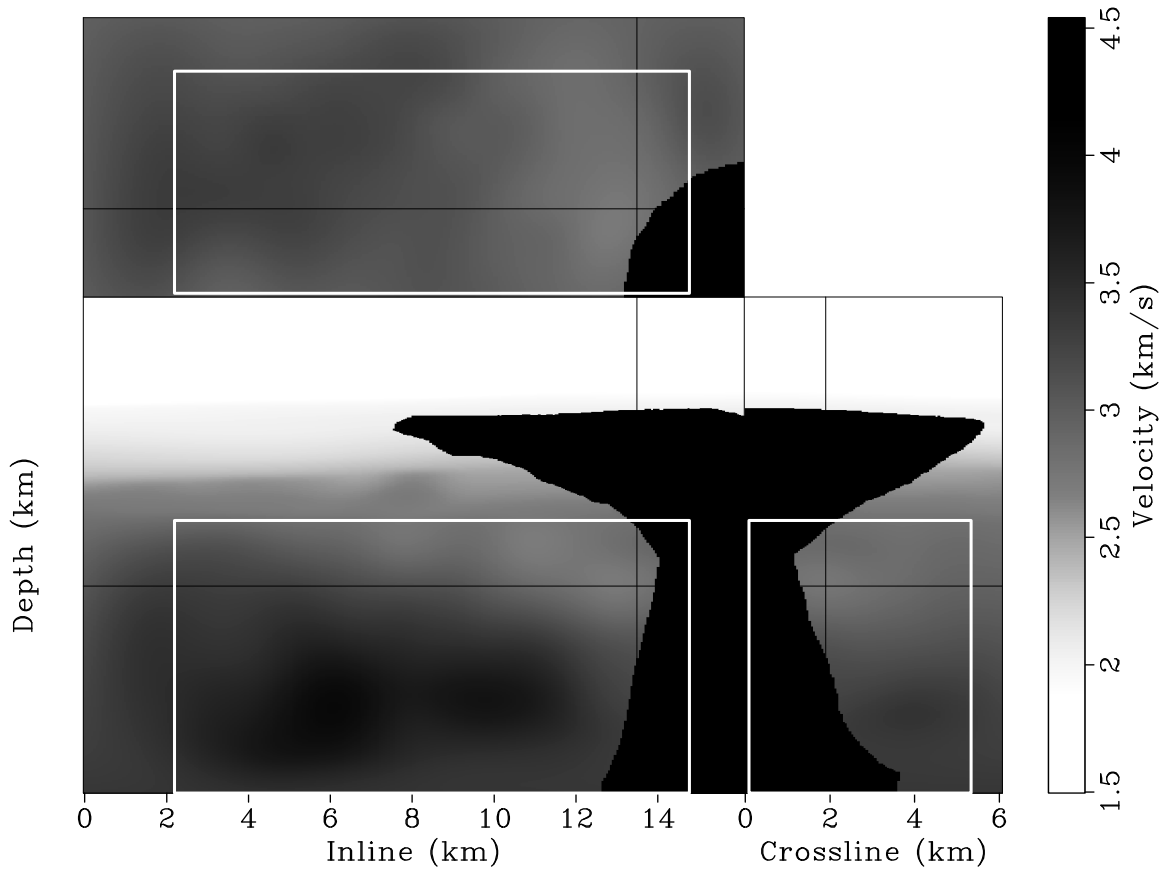


Figure 10: The final velocity model after merging the inverted velocity model in the target region with the velocity model above the target. [CR]

15 and 16 show the corresponding angle-domain common-image gathers (ADCIGs) before and after updating the velocity model. The flatness and coherence of ADCIGs have been improved considerably after updating the subsalt velocities.

CONCLUSIONS

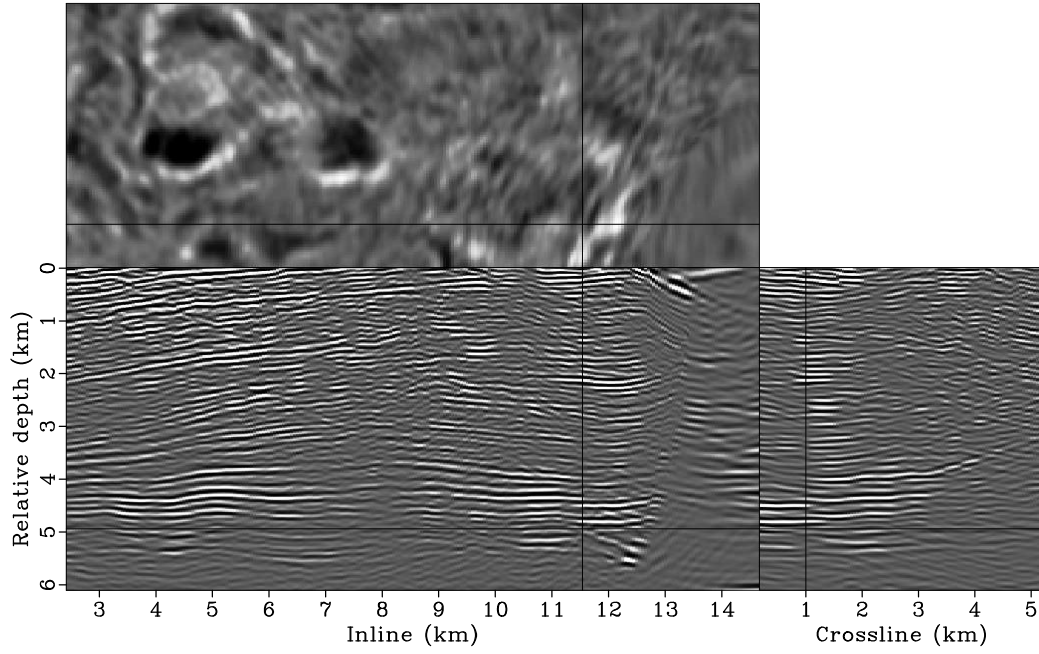
We have presented a methodology for performing image-domain wavefield tomography. Our method is extremely efficient, because we formulate the velocity estimation problem in a target-oriented fashion, and use a synthesized Born data set for velocity inversion. Our method is wavefield-based; therefore it is suitable for estimating velocities in complex geologies. Numerical examples on a 3-D field data set give excellent inversion results. The entire velocity analysis workflow can be fully automated, and no picking is necessary, although human interaction can be easily incorporated if it is desired. Thus our method provides a good tool for fast, accurate and flexible velocity model building in areas with complex geologies.

ACKNOWLEDGEMENTS

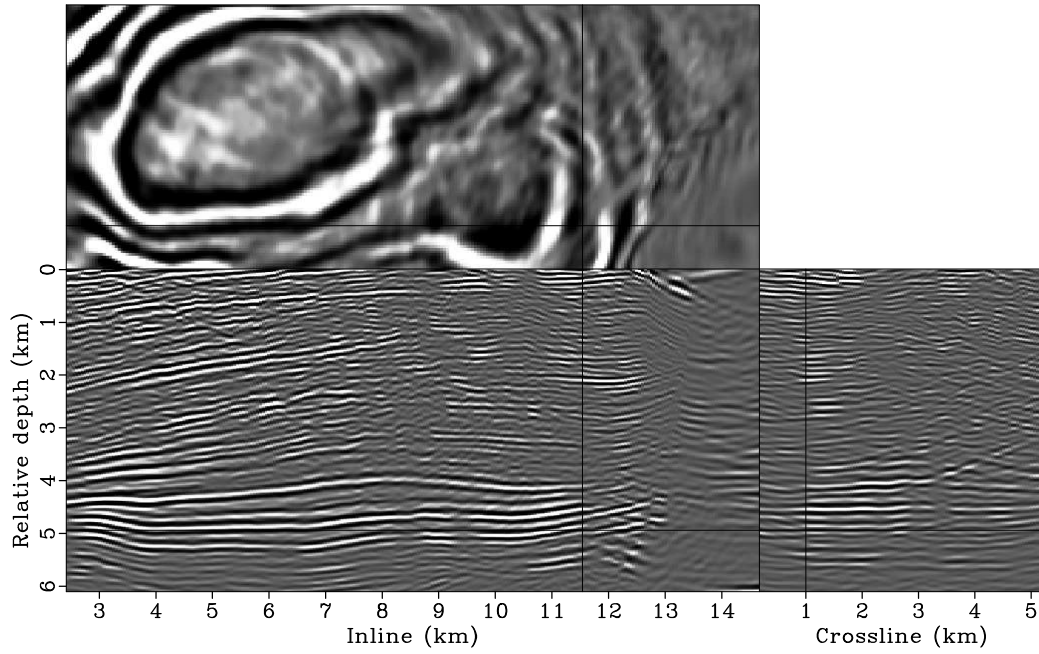
We thank BP and ExxonMobil for providing the field data set. We also thank the Stanford Center for Computational Earth and Environmental Science for providing computing resources.

REFERENCES

- Albertin, U., P. Sava, J. Etgen, and M. Maharramov, 2006, Adjoint wave-equation velocity analysis: SEG Technical Program Expanded Abstracts, **25**, 3345–3349.
- Biondi, B., 2006, Prestack exploding-reflectors modeling for migration velocity analysis: SEG Technical Program Expanded Abstracts, **25**, 3056–3060.
- Biondi, B., S. Fomel, and N. Chemingui, 1998, Azimuth moveout for 3-d prestack imaging: Geophysics, **63**, 574–588.
- Biondi, B. and P. Sava, 1999, Wave-equation migration velocity analysis: SEG Technical Program Expanded Abstracts, **18**, 1723–1726.
- Bleistein, N. and H. Jaramillo, H., 2000, A platform for Kirchhoff data mapping in scalar models of data acquisition: Geophysical Prospecting, **48**, 135–161.
- Bunks, C., F. M. Saleck, S. Zaleski, and G. Chavent, 1995, Multiscale seismic waveform inversion: Geophysics, **60**, 1457–1473.
- Duquet, B., P. Lailly, and A. Ehinger, 2001, 3d plane wave migration of streamer data: SEG Technical Program Expanded Abstracts, **20**, 1033–1036.
- Fei, W. and P. Williamson, 2010, On the gradient artifacts in migration velocity analysis based on differential semblance optimization: SEG Technical Program Expanded Abstracts, **29**, 4071–4076.

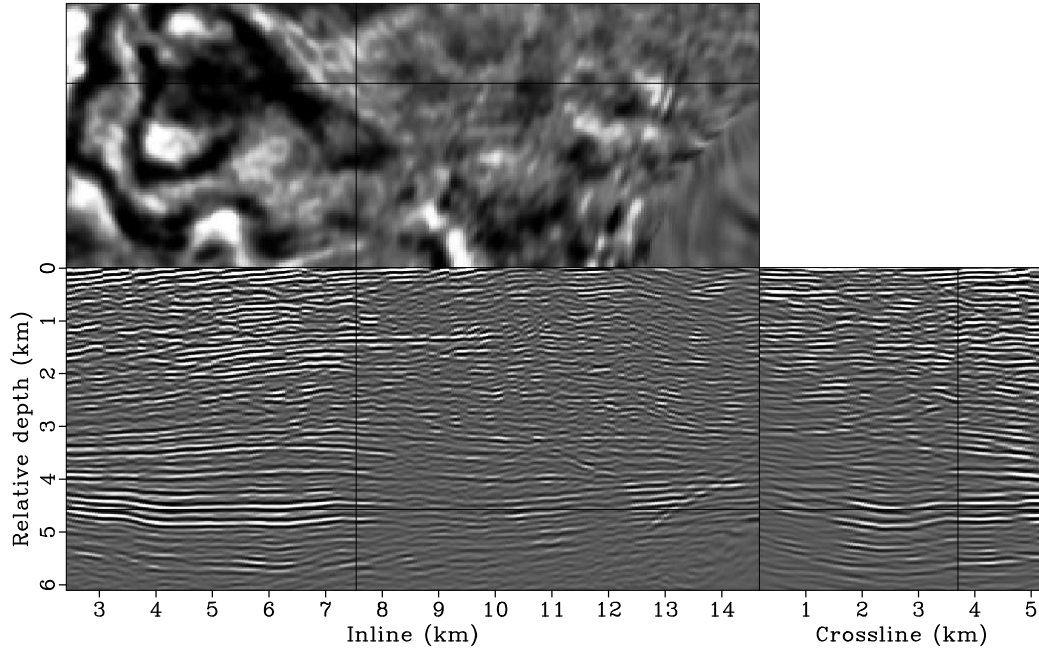


(a)

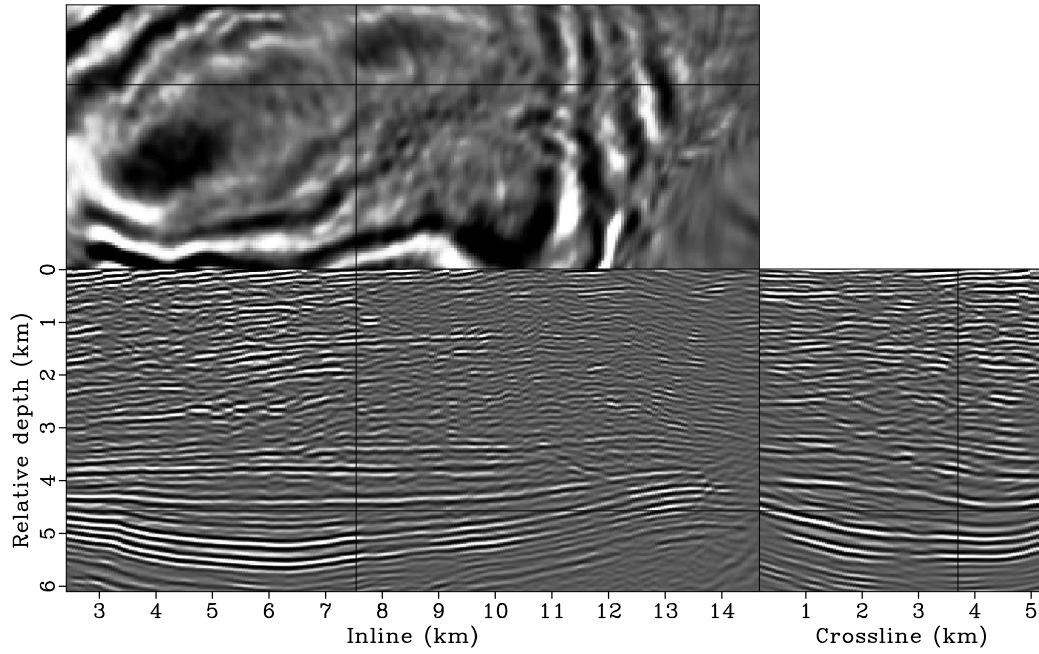


(b)

Figure 11: Comparison between the zero-subsurface-offset image (a) before and (b) after updating the velocities. Both results are obtained using the original surface-recorded data set. In both panels, the crosshair is taken at inline 11.55 km, crossline 1.00 km and relative depth 4.94 km. [CR]

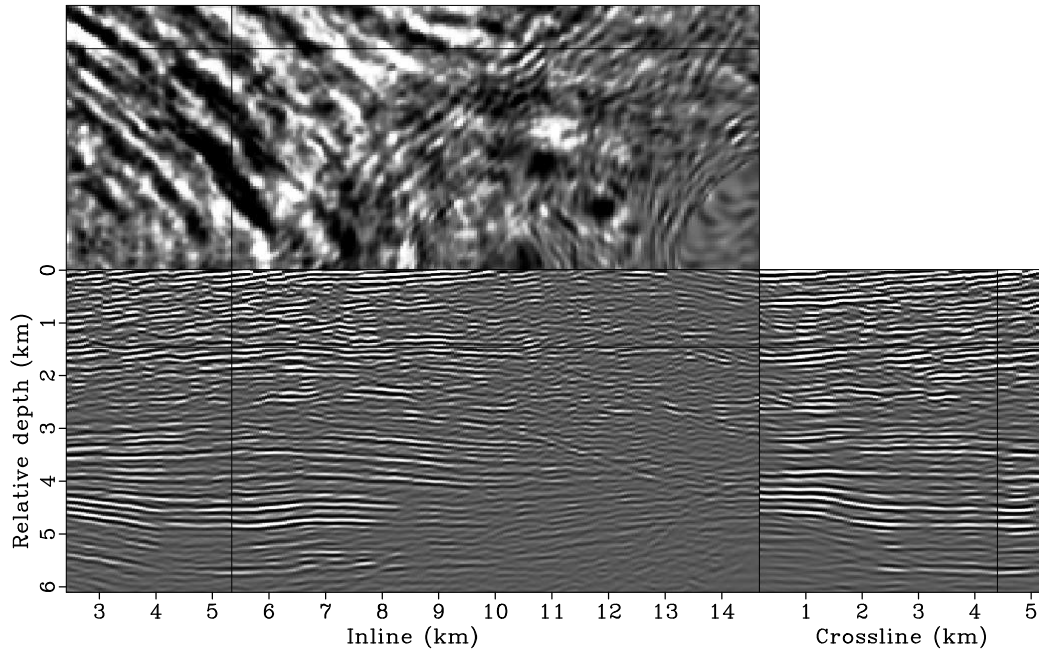


(a)

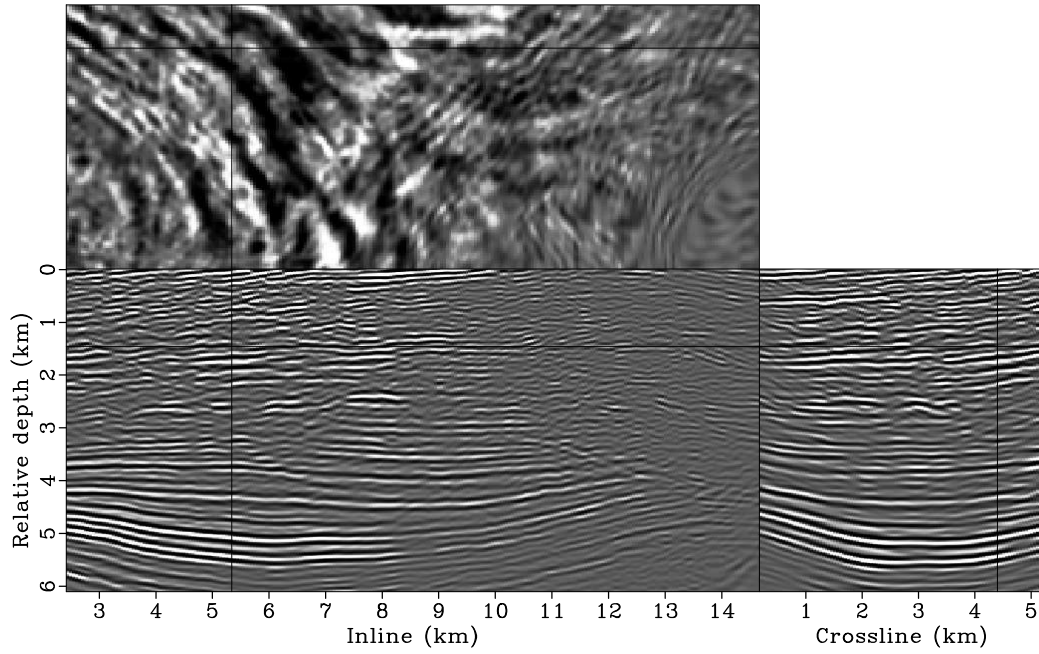


(b)

Figure 12: Comparison between the zero-subsurface-offset image (a) before and (b) after updating the velocities. Both results are obtained using the original surface-recorded data set. In both panels, the crosshair is taken at inline 7.55 km, crossline 3.70 km and relative depth 4.57 km. [CR]



(a)



(b)

Figure 13: Comparison between the zero-subsurface-offset image (a) before and (b) after updating the velocities. Both results are obtained using the original surface-recorded data set. In both panels, the crosshair is taken as inline 5.35 km, crossline 4.40 km and relative depth 1.46 km. [CR]

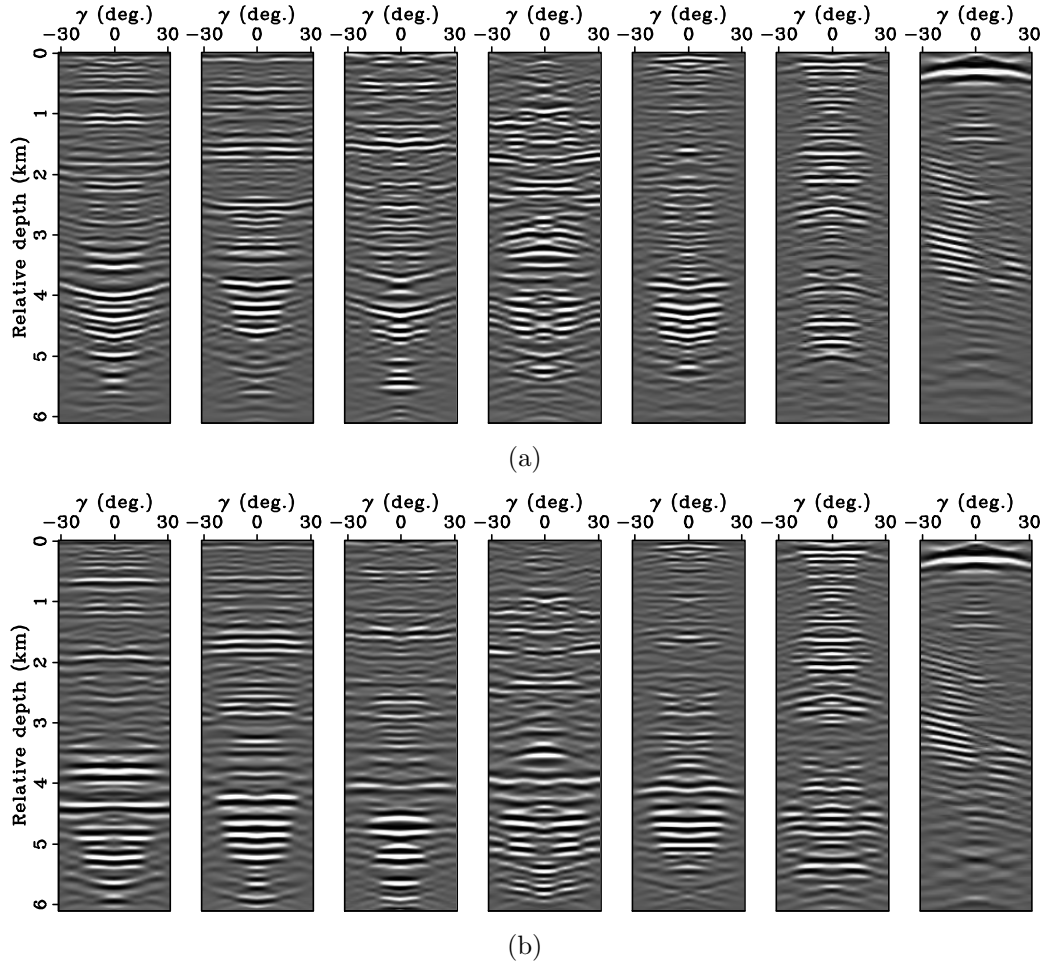


Figure 14: Comparisons between ADCIGs (a) before and (b) after updating the velocities. Both results are obtained using the original surface-recorded data set. All of the ADCIGs are extracted at the same crossline (1.00 km), but at inlines 1.52, 3.05, 4.57, 6.10, 7.62, 9.14 and 10.67 km, from left to right. [CR]

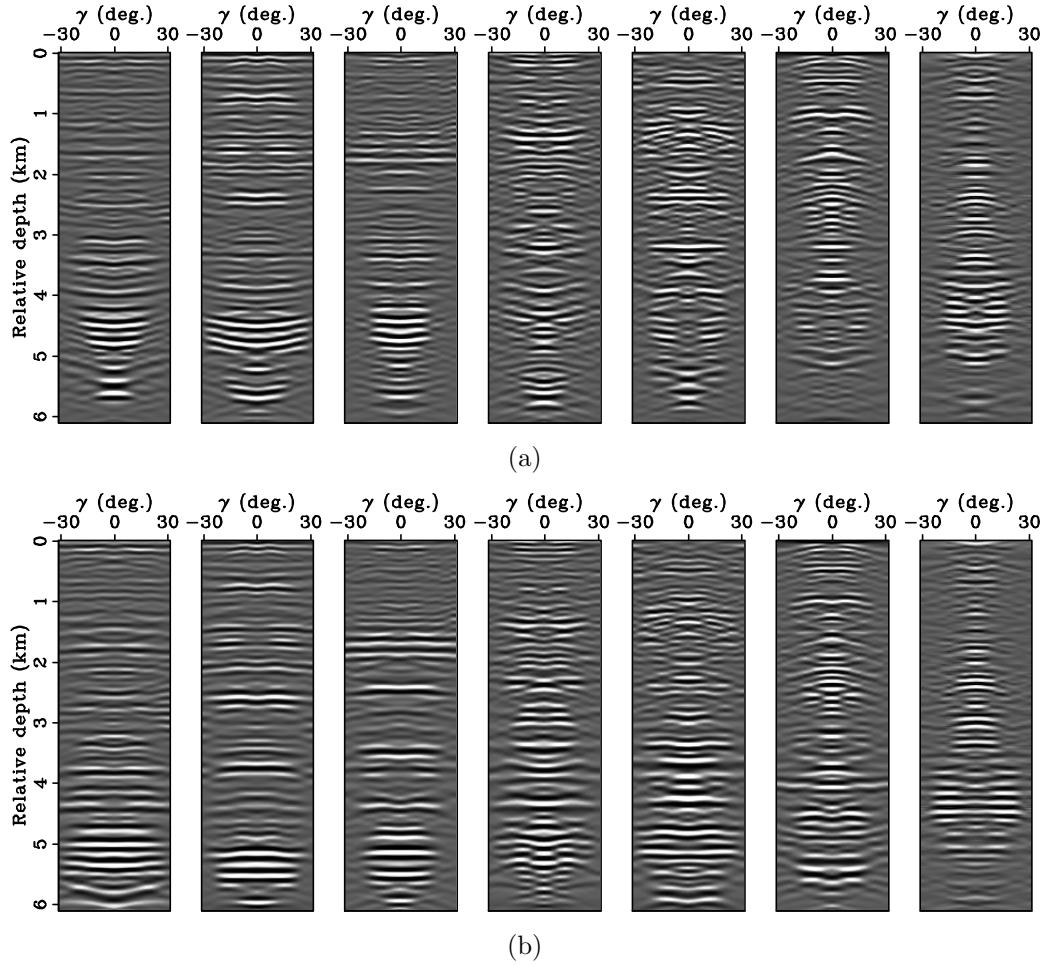


Figure 15: Comparisons between ADCIGs (a) before and (b) after updating the velocities. Both results are obtained using the original surface-recorded data set. All of the ADCIGs are extracted at the same crossline (3.70 km), but at inlines 1.52, 3.05, 4.57, 6.10, 7.62, 9.14 and 10.67 km, from left to right. [CR]

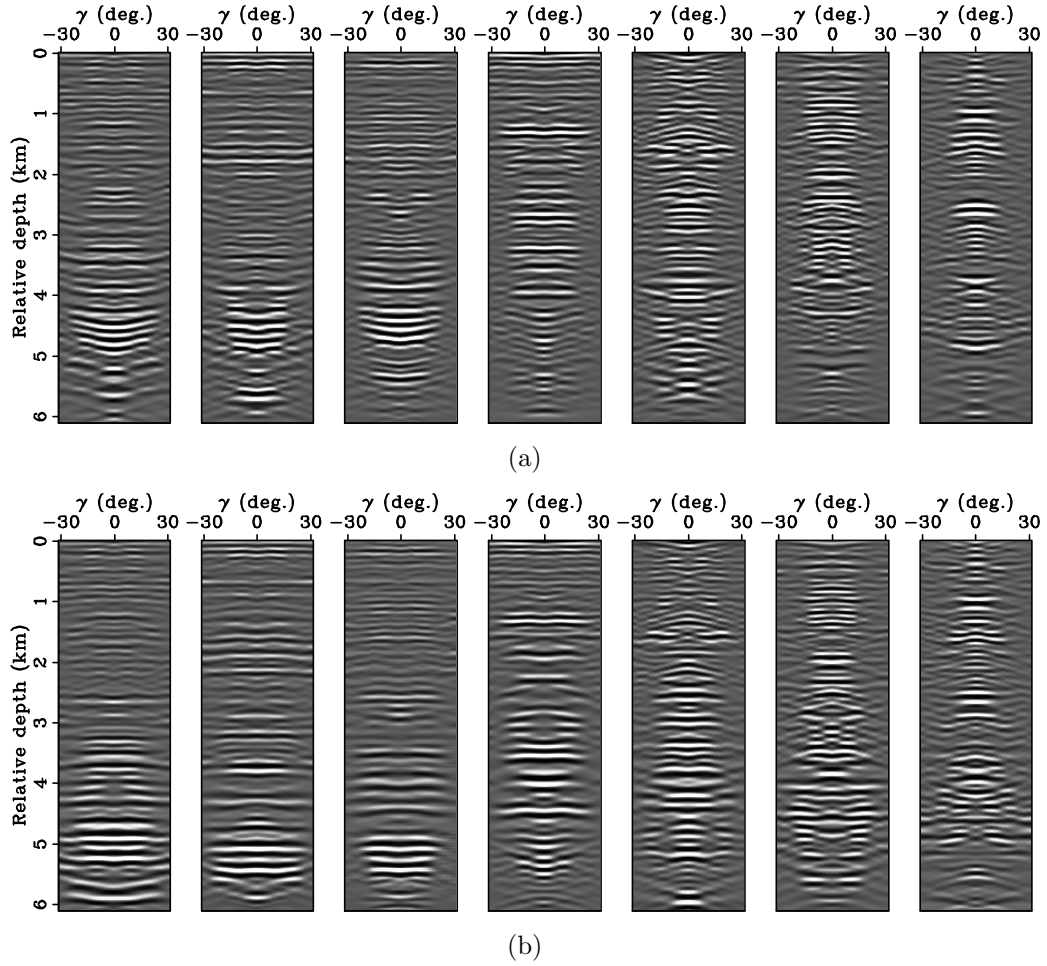


Figure 16: Comparisons between ADCIGs (a) before and (b) after updating the velocities. Both results are obtained using the original surface recorded data set. All of the ADCIGs are extracted at the same crossline (4.40 km), but at inlines 1.52, 3.05, 4.57, 6.10, 7.62, 9.14 and 10.67 km, from left to right. [CR]

- Fei, W., P. Williamson, and A. Khoury, 2009, 3-d common-azimuth wave-equation migration velocity analysis: SEG Technical Program Expanded Abstracts, **28**, 2283–2287.
- Guerra, C., 2010, Migration-velocity Analysis Using Image-space Generalized Wavefields: PhD thesis, Stanford University.
- Guerra, C., Y. Tang, and B. Biondi, 2009, Wave-equation tomography using image-space phase encoded data: SEG Technical Program Expanded Abstracts, **28**, 3964–3968.
- Halpert, A. D., R. G. Clapp, J. Lomask, and B. Biondi, 2008, Image segmentation for velocity model construction and updating: SEG Technical Program Expanded Abstracts, **27**, 3088–3092.
- Hubral, P., J. Schleicher, and M. Tygel, 1996, A unified approach to 3-D seismic reflection imaging, part I: Basic concepts: Geophysics, **61**, 742–758.
- Jin, S. and S. Xu, 2010, Visibility analysis for target-oriented reverse time migration and optimizing acquisition parameters: The Leading Edge, **29**, 1372–1377.
- Liu, F., D. W. Hanson, N. D. Whitmore, R. S. Day, and R. H. Stolt, 2006, Toward a unified analysis for source plane-wave migration: Geophysics, **71**, no. 4, S129–S139.
- Plessix, R.-E. and W. A. Mulder, 2004, Frequency-domain finite-difference amplitude-preserving migration: Geophys. J. Int., **157**, 975–987.
- Sava, P. and I. Vlad, 2008, Numeric implementation of wave-equation migration velocity analysis operators: Geophysics, **73**, VE145–VE159.
- Shen, P., 2004, Wave-equation Migration Velocity Analysis by Differential Semblance Optimization: PhD thesis, Rice University.
- Shen, P. and W. W. Symes, 2008, Automatic velocity analysis via shot profile migration: Geophysics, **73**, VE49–VE59.
- Shen, P., W. W. Symes, S. Morton, A. Hess, and H. Calandra, 2005, Differential semblance velocity analysis via shot profile migration: SEG Technical Program Expanded Abstracts, **24**, 2249–2252.
- Soubaras, R. and B. Gratacos, 2007, Velocity model building by semblance maximization of modulated-shot gathers: Geophysics, **72**, U67–U73.
- Stolt, R. H. and A. Benson, 1986, Seismic Migration: Theory and Practice: Geophysical Press.
- Symes, W. W. and J. J. Carazzone, 1991, Velocity inversion by differential semblance optimization: Geophysics, **56**, 654–663.
- Tang, Y., 2007, Selective stacking in the reflection-angle and azimuth domain: SEG Technical Program Expanded Abstracts, **26**, 2320–2324.
- , 2009, Target-oriented wave-equation least-squares migration/inversion with phase-encoded Hessian: Geophysics, **74**, WCA95–WCA107.
- Tang, Y. and B. Biondi, 2010, Target-oriented wavefield tomography using demigrated Born data: SEG Technical Program Expanded Abstracts, **29**, 4280–4285.
- , 2011, Subsalt imaging by target-oriented wavefield tomography: A 3-D field-data example: **SEP-143**, xxx–xxx.
- Tang, Y., C. Guerra, and B. Biondi, 2008, Image-space wave-equation tomography in the generalized source domain: **SEP-136**, 1–22.
- Tang, Y. and S. Lee, 2010, Preconditioning full waveform inversion with phase-

- encoded hessian: SEG Technical Program Expanded Abstracts, **29**, 1034–1038.
- Tarantola, A., 2005, Inverse problem theory: Methods for data fitting and model parameter estimation: Society for Industrial and Applied Mathematics.
- Valenciano, A., 2008, Imaging by Wave-equation Inversion: PhD thesis, Stanford University.
- Vyas, M. and Y. Tang, 2010, Gradients for wave-equation migration velocity analysis: SEG Technical Program Expanded Abstracts, **29**, 4077–4081.
- Whitmore, N. D., 1995, An Imaging Hierarchy for Common Angle Plane Wave Seismogram: PhD thesis, University of Tulsa.
- Zhang, Y., J. Sun, C. Notfors, S. H. Gray, L. Chernis, and J. Young, 2005, Delayed-shot 3d depth migration: Geophysics, **70**, E21–E28.